Supporting Information

Protection of Cobalt-free $LiNiO_2$ from Degradation with Localized Saturated Electrolytes in Lithium-metal Batteries

Laisuo Su, Eunmi Jo, Arumugam Manthiram*

Materials Science and Engineering Program & Texas Materials Institute, The University of Texas at Austin, Austin, TX 78712, United States

Corresponding Author: manth@austin.utexas.edu

Experimental Methods:

Materials preparation. The baseline electrolyte was LP57 + 2% vinylene carbonate (VC, Gotion, purity 99.98%). The LP57 electrolyte consisted of 1 M lithium hexafluorophosphate ($LiPF_6$) in a solvent containing 3:7 weight ratio of ethylene carbonate (EC) and ethyl methyl carbonate (EMC). The saturated-concentration electrolyte (SE) consisted of 3 M $LiPF_6$ (Gotion, purity 99.9%) dissolved in a solvent containing 3:7 weight ratio of EC (Gotion, purity 99.96%) and EMC (Gotion, purity 99.72%). The localized saturated electrolyte (LSE) was prepared by adding 1,1,2,2-tetrafluoroethyl-2,2,3,3-tetrafluoropropyl ether (TTE, SynQuest, purity 99%) into the SE electrolyte with a volume ratio of 2:1. The hydroxide precursor of the $LiNiO_2$ powder was obtained with an in-house coprecipitation process.[1] The precursor was mixed with $LiOH{\cdot}H_2O$ at a molar ratio of 1:1.03, followed by a heating treatment at 655 ^oC for 12 h. The calcinated cathode material was then mixed with conductive carbon black (Super P), and the polyvinylidene fluoride binder in N-methyl-2-pyrrolidone with a weight ratio of 90:5:5. The resulting slurry was cast onto an Al foil with an active material loading of ~ 9 mg cm^{-2}, and the thickness of the cathode is ~ 35 μm. The cathode electrode was dried in a vacuum furnace at 110 ^oC overnight before assembling the cells.

Materials characterization. The conductivities of the three electrolytes were measured via a conductivity meter (Mettle-Toledo SevenCompact S230). Fourier transform infrared (FTIR) spectra of different solvents and electrolytes were collected to study the solvation structure of the electrolytes with a Thermofisher FTIR Spectrometer equipped with an attenuated total reflection attachment and a germanium crystal. FTIR spectra were collected from 400 cm^{-1} to 4,000 cm^{-1} at a 0.5 cm^{-1} resolution and averaged

over 35 scans. Raman spectroscopic data of the electrolytes were carried out with a Witec Micro-Raman Spectrometer Alpha 300 with a visible Raman microscope and a CCD detector. The excitation wavelength was 532 nm and the spectra were collected over 60 s at ~ 3.0 cm^{-1} resolution. Scanning electron microscope (SEM, FEI Quanta 650) images of synthesized $LiNiO_2$ particles were collected to confirm the particle size. A laboratory Cu Kα X-ray source was used to characterize the crystal structure of $LiNiO_2$ powder from 10^o to 80^o with a 0.02^o scan step (Rigaku Miniflex 600). X-ray photoelectron spectroscopy (XPS) measurements were collected on cycled $LiNiO_2$ electrodes with a Kratos Axis Ultra DLD spectrometer with an Al Kα radiation (1486.6 eV) excitation source. Aged cells were disassembled inside an Argon-filled glovebox to harvest the electrode samples, which were loaded into an in-house transfer chamber (patent number US9945761) inside the glovebox to avoid air exposure during sample transfer. Regions scans were performed with a step size of 0.1 eV. CasaXPS software was utilized to deconvolute the peaks by fitting the experimental data with multiple Gaussian-Lorentzian functions after a Shirley background correction. The adventitious carbon peak at 248.8 eV was used for calibration. Transmission electron microscope (TEM) images of aged $LiNiO_2$ electrodes were obtained to investigate the structural changes on the surface. Cycled $LiNiO_2$ cathode was washed with dimethyl carbonate (DMC) solution to remove the residual salts. The $LiNiO_2$ powder was then scratched gently from the electrode and then sonicated in DMC. The dispersed $LiNiO_2$ powder in the solution was dropped onto a lacey-carbon TEM grid. All the sample preparations were performed inside an Ar-filled glovebox to avoid exposure to air and moisture. Electron energy loss spectroscopy (EELS) line scanning was conducted to

investigate the change of the oxidation state of oxygen and nickel on the surface of the electrodes.

Electrochemical tests. CR2032-type coin cells were assembled inside an Argon-fill glovebox with an O_2 and H_2O level below 1 ppm. $LiNiO_2$ cathode, Celgard 2325 separator, and Li-metal anode (~ 400 μm) were sandwiched together with 100 μl electrolyte and crimped within the coin cell casings. Cyclic voltammetry (CV) scans were recorded with a Biologic VMP3 potentiostat from 2.8 to 4.4 V with scan rates of 0.05 mV s^{-1}, 0.1 mV s^{-1}, 0.2 mV s^{-1}, and 0.4 mV s^{-1}. Cycling tests were carried out with an Arbin battery test station. The cells were cycled at C/10 (1C = 180 mA g^{-1}) rate from 2.8 to 4.4 V three times before conducting the cycling tests. Electrochemical impedance spectroscopy was carried out by applying an AC voltage of 10 mV amplitude over the frequency range of 1 MHz to 10 mHz at an open-circuit voltage of 3.8 V with a Solartron SI 1287 potentiostat. The self-discharge test was carried out with an Arbin battery test station. Fully charged cells were stored inside an ESPEC BTZ-133 environmental chamber at 45 ^oC for 100 h, followed by a discharge at a C/10 rate to 2.8 V.

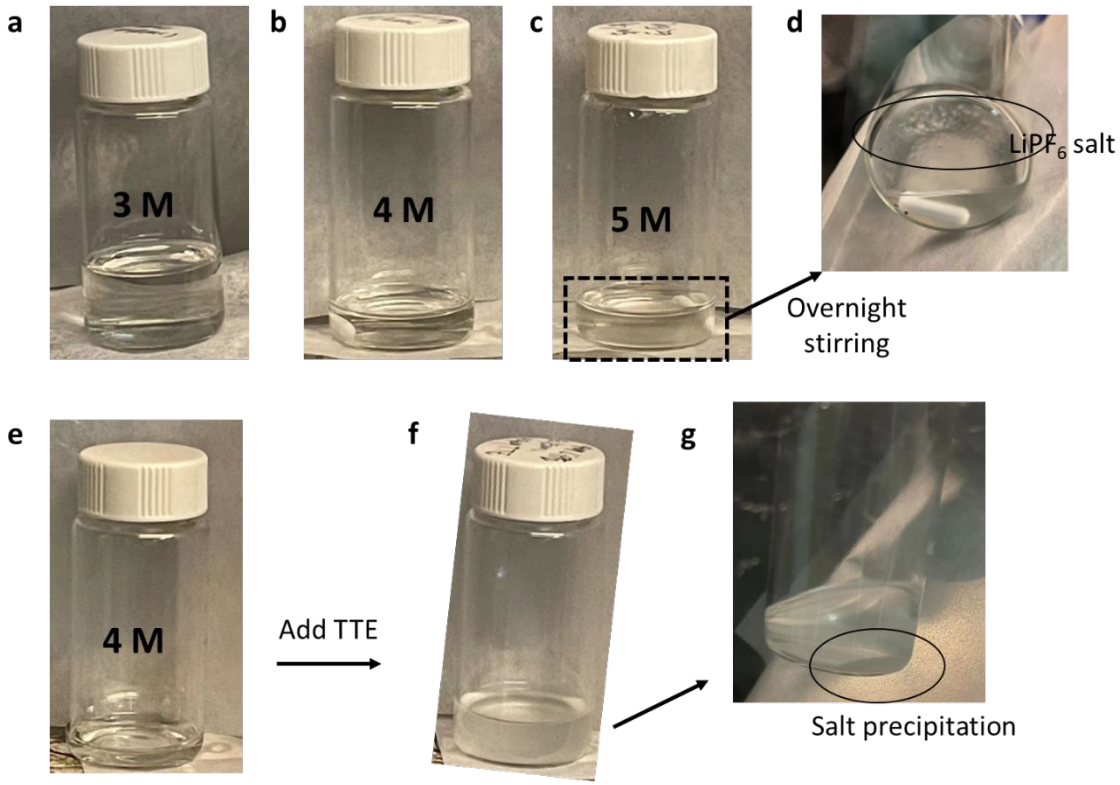

Figure S1. Test the solubility of $LiPF_6$ in carbonate solvents (EC/EMC 3/7 by weight). (a-c) $LiPF_6$ salt dissolves in EC/EMC solution with a salt concentration of 3 M (a), 4 M (b), and 5 M (c). (d) Some $LiPF_6$ salt cannot be dissolved in the 5 M solution even after overnight stirring. (e-g) The change of the 4 M $LiPF_6$ solution after adding TTE diluent. Some salts precipitate out from the solution after adding TTE (g).

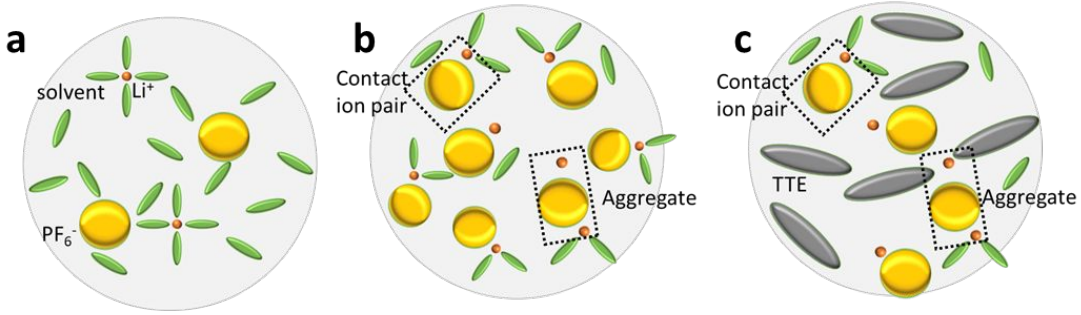

Figure S2. Schematics showing the solvation structure of (a) LP57 electrolyte, (b) $LiPF_6$-based saturated electrolyte, and (c) $LiPF_6$-based localized saturated electrolyte.

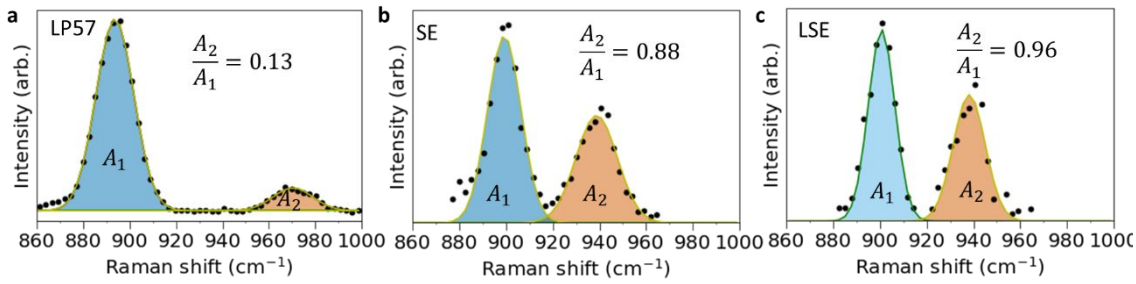

Figure S3. Raman spectra of the three electrolytes in the region ranging from 860 to 1,000 cm^{-1}. The Gaussian function was applied to fit the two peaks in this region and the ratio of the areas under the two peaks was determined by the integrated intensities.

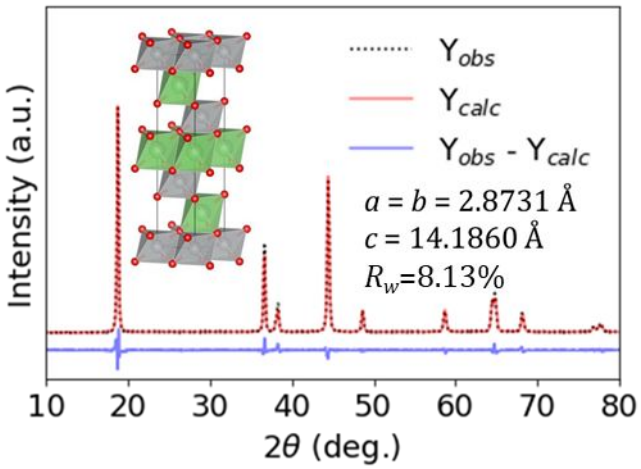

Figure S4. Rietveld refinement of the $LiNiO_2$ powder XRD data and schematic structure of the layered $LiNiO_2$.

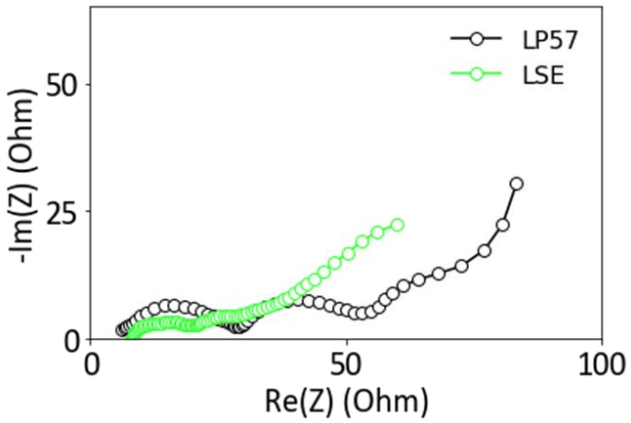

Figure S5. Comparison of the electrochemical impedance spectra of Li|$LiNiO_2$ cells with the LP57 electrolyte and LSE after the rate test.

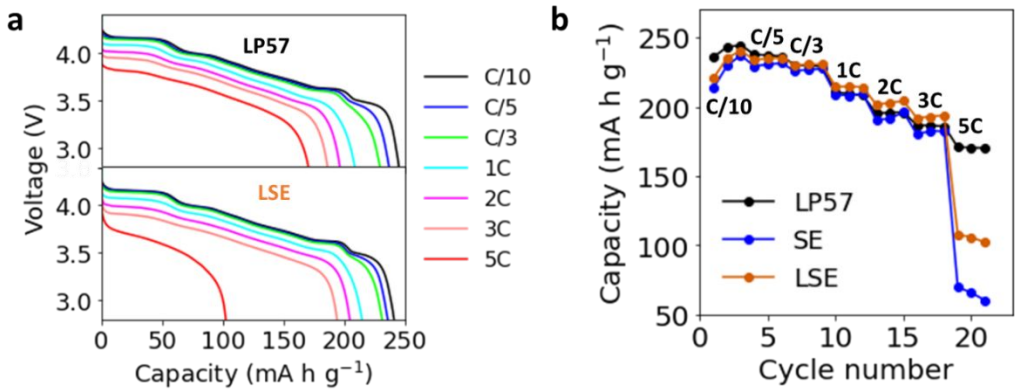

Figure S6. The rate capability of $LiNiO_2$ tested in different electrolytes. (a) Discharge curves of $LiNiO_2$ at different C rates with the LP57 electrolyte and the LSE. (b) Discharge capacities of $LiNiO_2$ in the three electrolytes, where the charge rate was C/5.

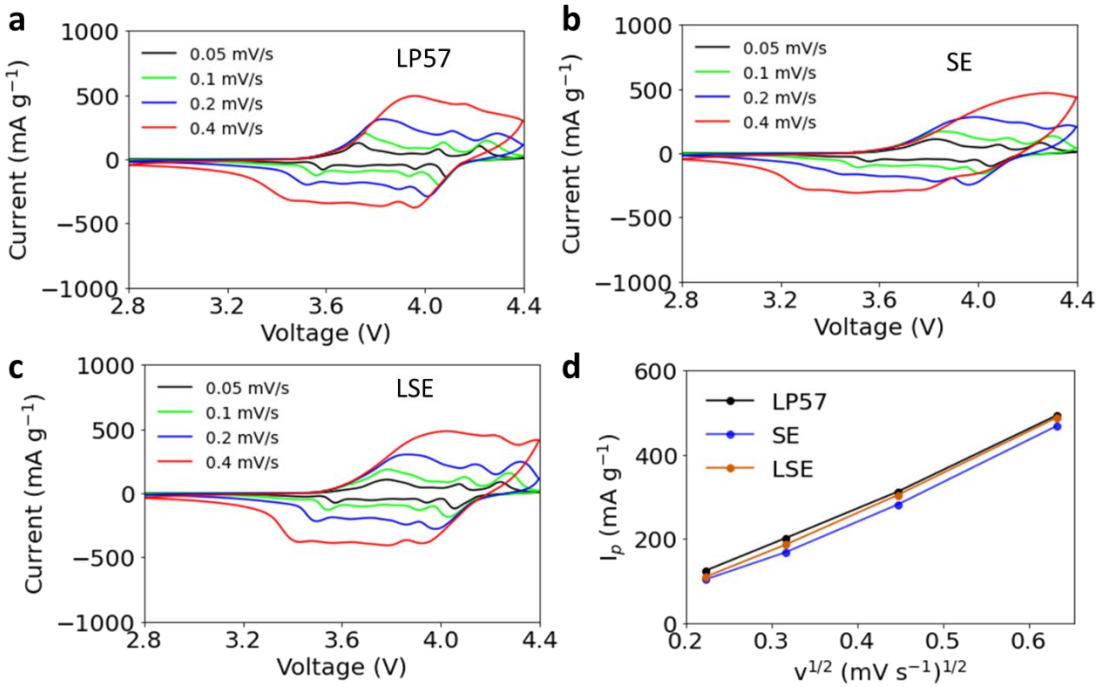

Figure S7. Cyclic voltammetry (CV) measurement of $LiNiO_2$ electrode. (a-c) CV measurement results with different scan rates for the $LiNiO_2$ electrode tested in the LP57 electrolyte (a), SE (b), and LSE (c). The scan rates are 0.05 mV s^{-1}, 0.1 mV s^{-1}, 0.2 mV s^{-1}, and 0.4 mV s^{-1}. (d) Relationship between the peak current and the scan rate of the $LiNiO_2$ electrodes with three different electrolytes.

Li^+ diffusion coefficients calculated from the CV scan for electrolytes

In a diffusion-controlled scenario, the peak current can be expressed as follows during a CV scan experiment:

$$i_p = 2.69 \times 10^5 n^{3/2} S D^{1/2} v^{1/2} C \quad \text{(S1)}$$

where n is the number of electrons transferred, S is the electrode surface area, C is the Li^+ concentration, v is the CV scan rate, and D is the Li^+ diffusion coefficient in the electrolyte.

The slope can be correlated to the D as

$$slope = \frac{i_p}{v^{1/2}} = 2.69 \times 10^5 n^{3/2} S D^{1/2} C \quad \text{(S2)}$$

$$D = \left(\frac{slope}{2.69 \times 10^5 n^{3/2} S C} \right)^2 \quad \text{(S3)}$$

In the SE, the Li^+ concentration is around 3 times higher than that in the LP57 electrolyte and LSE. A similar slope value in Figure S7d indicates that the Li^+ diffusion coefficient in SE is around 9 times smaller than that in the LP57 electrolyte and LSE, assuming the surface area (S) is the same for all electrolytes.

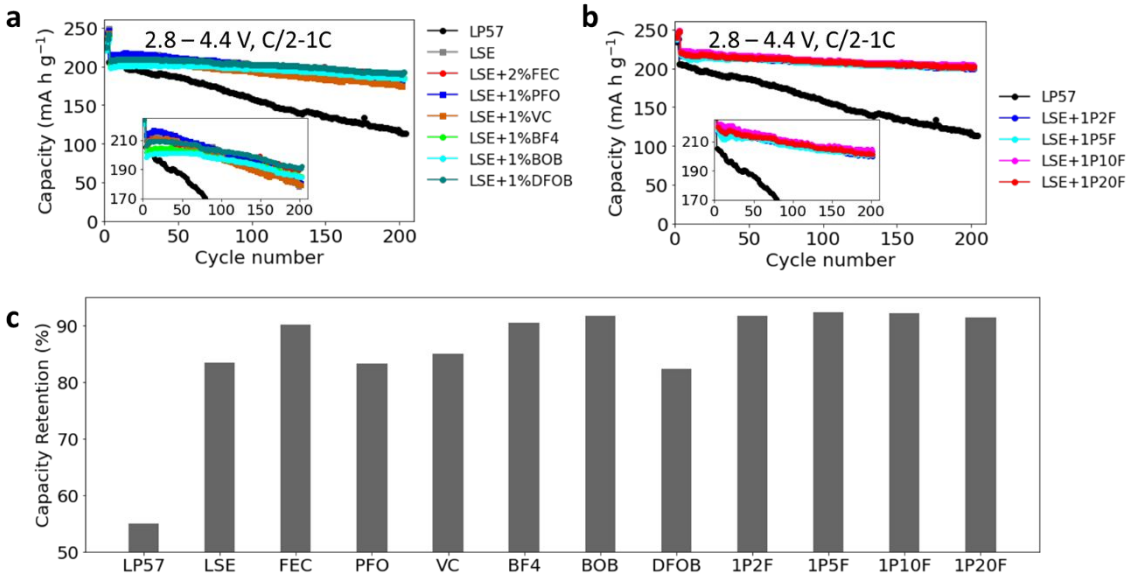

Figure S8. Effect of additives in the LSE on the electrochemical performance of $LiNiO_2$. (a) Effect of adding a single additive into the LSE on the cycling performance of $LiNiO_2$. The insert zooms into a limited capacity region to show the difference among these additives. (b) Effect of adding two additives into the LSE on the cycling performance of $LiNiO_2$. The 1P stands for 1% $LiPO_2F_2$*, and the xF stands for x% of FEC. (c) Comparing the effect of additives on the maximum cell capacity and the cell capacity retention after 200 cycles.

Abbreviations: FEC: fluoroethylene carbonate, PFO: lithium phosphorodifluoridate, VC: vinylene carbonate, BF4: lithium tetrafluoroborate, BOB: lithium bis(oxalato)borate, DFOB: lithium difluoroborate.

* The solubility of some additives, such as $LiPO_2F_2$ and LiDFOB, in the EC/EMC solvent is low and cannot be dissolved even 1% by weight. These additives were added into the LSE based on the calculated weight percentage, followed by an overnight stirring. After storing over 2 h, the clear solution was taken out and used as the electrolyte.

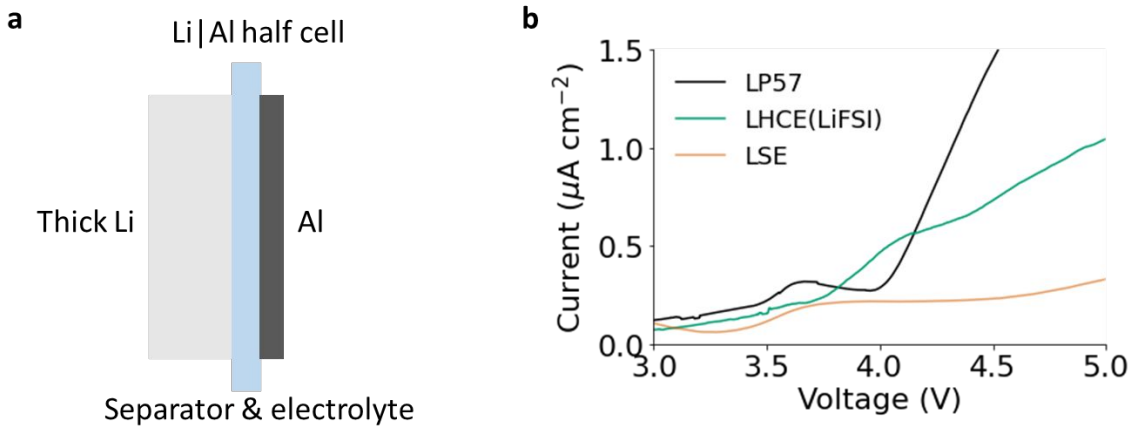

Figure S9. Anodic stability of different electrolytes tested via linear sweep voltammetry. (a) A schematic of the test cells. (b) the measured current density with respect to the voltage. The scan rate is 0.05 mV s^{-1}.

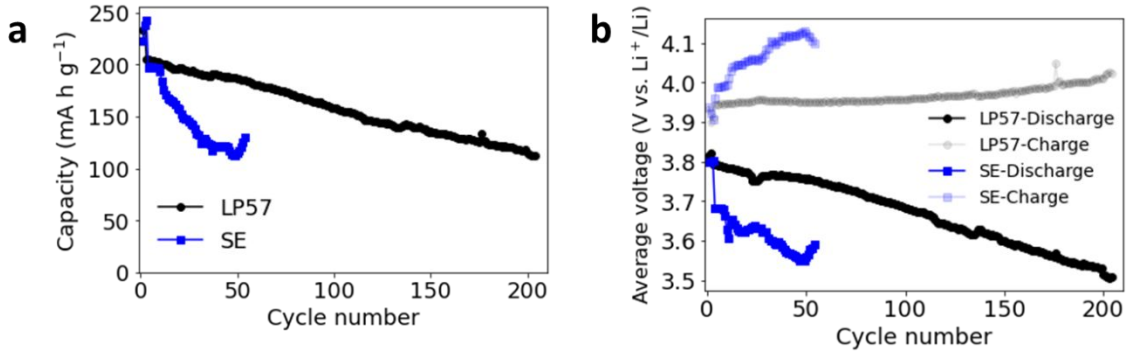

Figure S10. The cycling performance of Li|$LiNiO_2$ cells with the saturated electrolyte. (a) The cycling stability with the SE and the LP57 electrolyte tested at C/2 charge rate and 1C discharge rate. (b) Evolution of average charge and discharge voltages of cells.

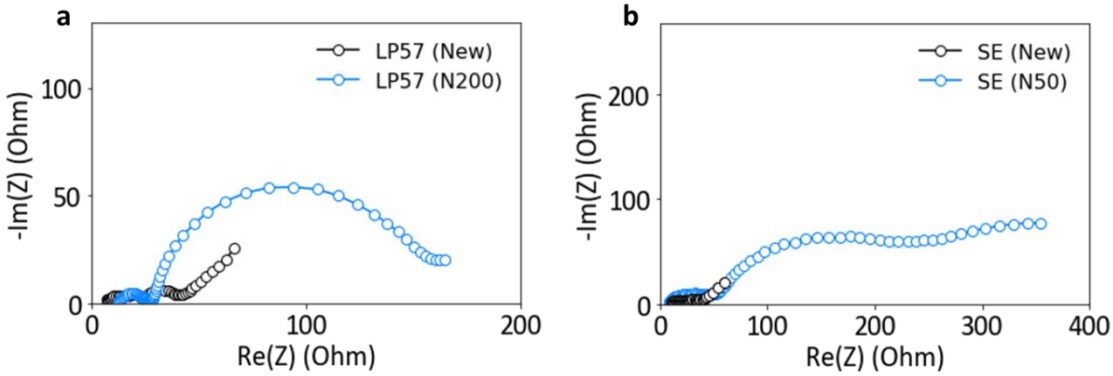

Figure S11. Evolution of the electrochemical impedance spectra of Li|$LiNiO_2$ cells with (a) the LP57 electrolyte and (b) the SE. N200 represents after 200 cycles, and N50 represents after 50 cycles.

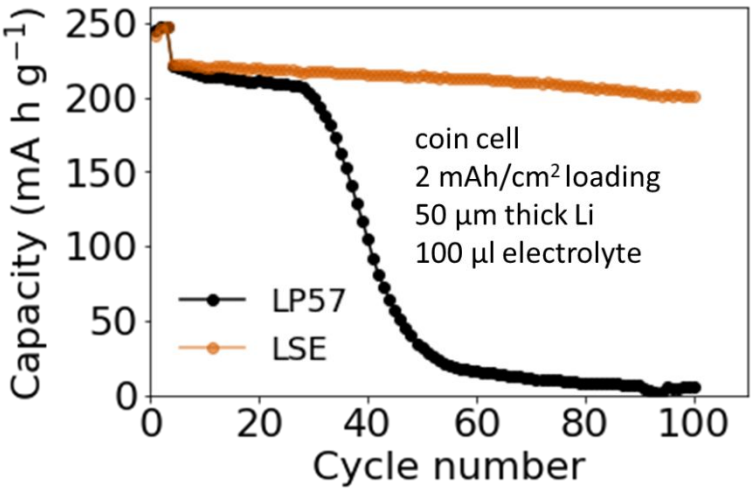

Figure S12. The applicability of the $LiPF_6$-based LSE in Li|$LiNiO_2$ cells tested with a 50 µm thick Li metal as the anode.

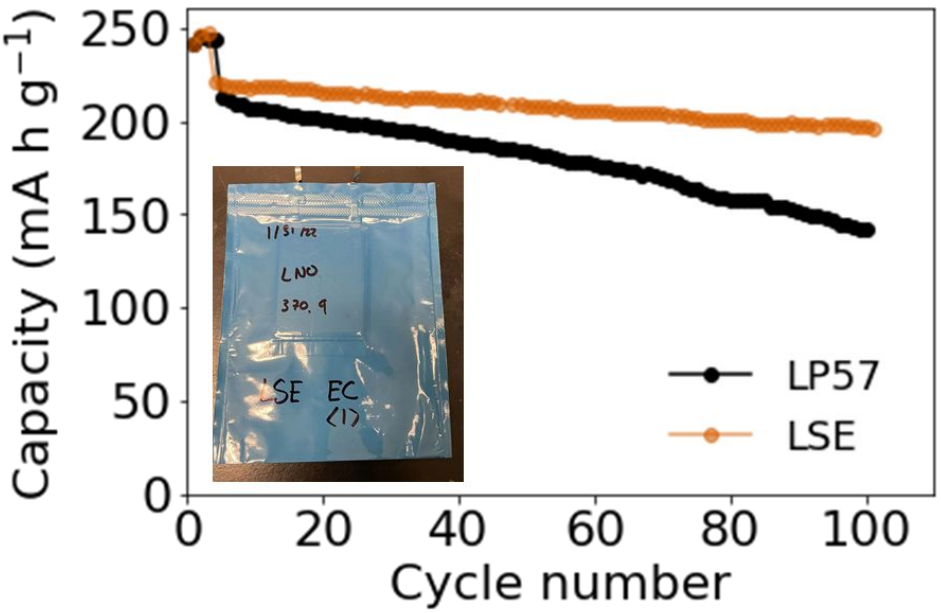

Figure S13.The applicability of the $LiPF_6$-based LSE tested in a single-layer pouch cell with Li metal as the anode and $LiNiO_2$ as the cathode.

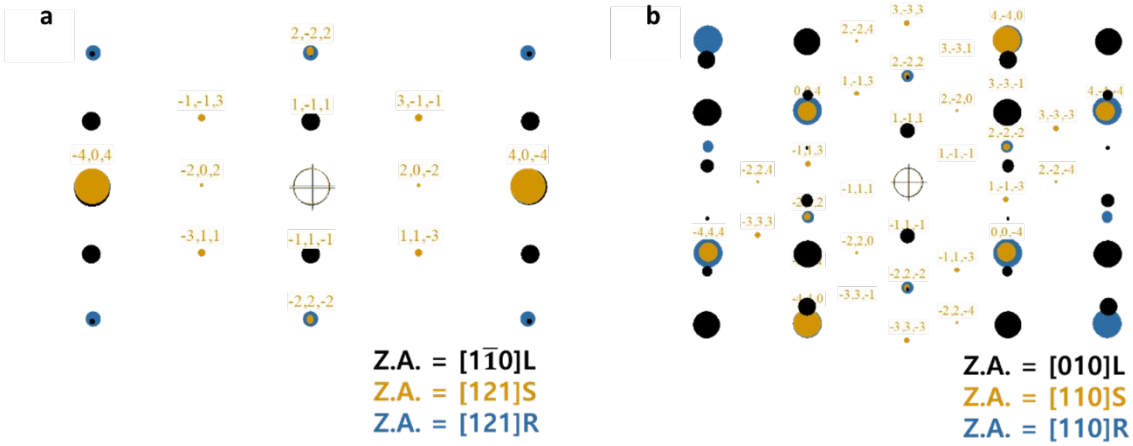

Figure S14. Simulated electron diffraction patterns of cycled $LiNiO_2$ cathode in the LP57 (a) and the LSE electrolytes (b). L = layered (black), S = spinel-like (yellow), and R = rock-salt structures (blue).

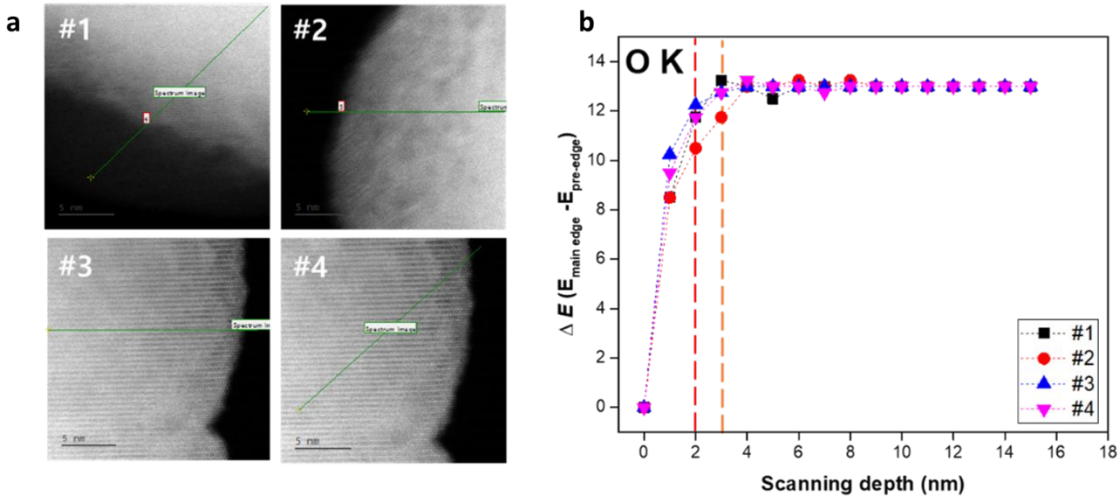

Figure S15. TEM images of $LiNiO_2$ particles. (a) TEM images of four more particles after 200 cycles with the LSE. (b) STEM-EELS line scanning data of the additional $LiNiO_2$ particles.

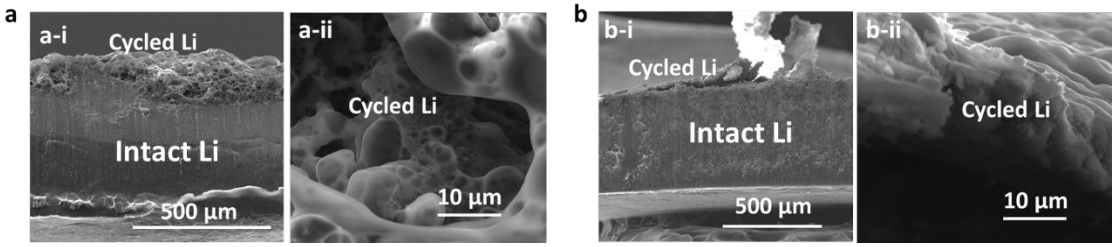

Figure S16. Cross-section SEM images of cycled Li metal in the (a) LP57 electrolyte and (b) LSE. Images with two different scales are shown to present the thickness and morphology of the cycled lithium-metal anode.

References

(1) Cui, Z.; Xie, Q.; Manthiram, A. Zinc-Doped High-Nickel, Low-Cobalt Layered Oxide Cathodes for High-Energy-Density Lithium-Ion Batteries. *ACS Appl. Mater. Inter.* **2021**, *13*, 15324-15332.